

Predicted T-XY ($X \neq Y = \text{P, As and Sb}$) monolayer with intrinsic persistent spin helix and large piezoelectric response

San-Dong Guo¹, Xu-Kun Feng², Dong Huang¹, Shaobo Chen³ and Yee Sin Ang²

¹*School of Electronic Engineering, Xi'an University of Posts and Telecommunications, Xi'an 710121, China*

²*Science, Mathematics and Technology (SMT), Singapore University of Technology and Design (SUTD),*

8 Somapah Road, Singapore 487372, Singapore and

³*College of Electronic and Information Engineering, Anshun University, Anshun 561000, People's Republic of China*

The persistent spin helix (PSH) is robust against spin-independent scattering and renders an extremely long spin lifetime, which can improve the performance of potential spintronic devices. To achieve the PSH, a unidirectional spin configuration is required in the momentum space. Here, T-XY ($X \neq Y = \text{P, As and Sb}$) monolayers with dynamical, mechanical and thermal stabilities are predicted to intrinsically possess PSH. Due to the C_{2v} point-group symmetry, a unidirectional spin configuration is preserved in the out-of-plane direction for both conduction and valence bands around the high-symmetry Γ point. That is, the expectation value of the spin S only has the out-of-plane component S_z . The application of an out-of-plane external electric field can induce in-plane components S_x and S_y , thus offering a promising platform for the on-off logical functionality of spin devices. T-XY ($X \neq Y = \text{P, As and Sb}$) monolayers are determined to be excellent two-dimensional (2D) piezoelectric materials. The in-plane piezoelectric coefficient d_{11} (absolute value) of T-SbP is 226.15 pm/V, which is larger than that reported for most 2D materials, providing possibility of tuning spin-splitting of PSH by in-plane electric field induced with a uniaxial in-plane strain through piezoelectric effect. Our work reveals a new family of T-phase 2D materials, which could provide promising applications in spintronic and piezoelectric devices.

Keywords: Spin-orbital coupling, Persistent spin helix, Piezoelectricity

Email:sandongyuwang@163.com

I. INTRODUCTION

In a material with broken inversion symmetry, the spin-orbital coupling (SOC) induces momentum (k)-dependent spin-orbit field (SOF), which can lift Kramer's spin degeneracy and leads to the nontrivial k -dependent spin textures of the spin-split bands through Rashba and Dresselhaus effects^{1,2}. Practically, the strong Rashba SOC allows for electrostatic manipulation of the spin states, which has potential application for non-charge-based computing and information processing³⁻⁵. However, strong SOC can cause spin decoherence, which leads to the reduced spin lifetime. The impurities and defects can change the momentum of electrons in a diffusive transport regime, and simultaneously randomize the spin due to the k -dependent SOF, which induces spin decoherence through the Dyakonov-Perel (DP) mechanism and limits the performance of potential spintronic devices⁶.

To overcome spin dephasing, a possible way is designing a structure with the SOF orientation to be unidirectional, which can preserve a unidirectional spin configuration in the k space. The unidirectional SOF will lead to a spatially periodic mode of the spin polarization, which is known as the persistent spin helix (PSH)^{7,8}. The spin dephasing can be suppressed by PSH due to SU(2) spin rotation symmetry, which renders an extremely long spin lifetime^{7,9}. The PSH has been demonstrated on various quantum well (QW) heterostructures, interface and surface¹⁰⁻¹⁶. Recently, a different approach for achieving the PSH is imposing the specific symmetry of the crystal, which has been realized in bulk-, layered- and

two-dimensional (2D)-ferroelectric systems¹⁷⁻²⁷. However, the search for 2D materials with intrinsic PSH has lately been very demanding of attention due to their potential for miniaturization spintronic devices.

If a material possesses broken inversion symmetry, it should be piezoelectric. The piezoelectricity represents the coupling between electric polarization and strain/stress. For 2D systems, the MoS₂ monolayer is theoretically predicted to a piezoelectric material²⁸, and then is proved experimentally²⁹. Theoretically, a large number of 2D materials have been predicted to be piezoelectric³⁰⁻³⁸. The SOF is proportional to electric field \vec{E} originated from the crystal inversion asymmetry^{39,40}. In fact, the SOF can be tuned by external electric field, which can be induced by strain through piezoelectric effect. So, the spin-splitting of PSH can be regulated by piezoelectric effect, which provides an alternative way for designing spintronic devices.

Recently, a unique phase of MX (M=Sn and Ge; X=S and Se), called the Tricycle-phase (T-phase), is proposed, and these T-MX monolayers possess fine piezoelectric performance and stability⁴¹. Here, keeping number of valence electrons of system to be constant, the T-XY ($X \neq Y = \text{P, As and Sb}$) monolayers are proposed, which are dynamically, mechanically and thermally stable. The T-XY are predicted to intrinsically possess PSH with a unidirectional out-of-plane spin configuration (S_z) for both conduction and valence bands due to the C_{2v} point-group symmetry. When an out-of-plane external electric field is applied, the in-plane components S_x and S_y can be induced, which offers a promising platform for the on-off logical functionality of spin devices. It is predicted

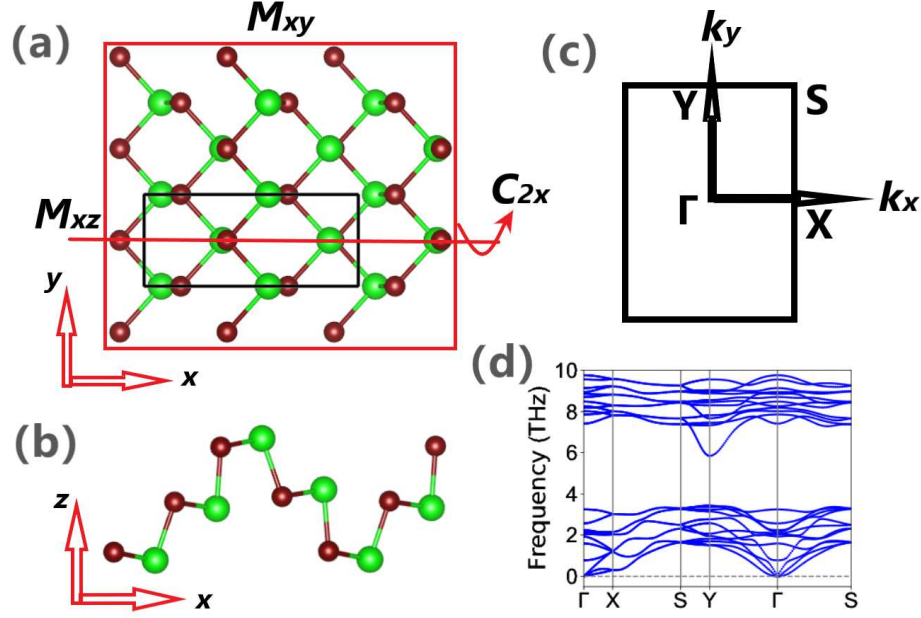


FIG. 1. (Color online) For monolayer T-XY ($X \neq Y = \text{P, As and Sb}$), the top view (a) and side view (b) of crystal structure with large balls for X atoms and small balls for Y atoms, and the related symmetry operations are shown in (a). The (c) and (d) show the first Brillouin zone with high-symmetry points, and phonon dispersion curves of T-SbP monolayer, respectively.

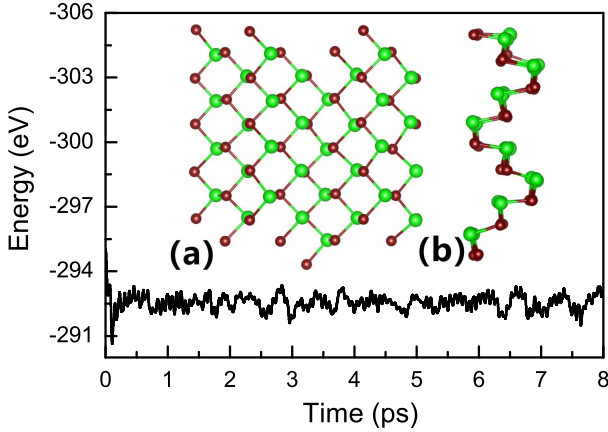


FIG. 2. (Color online) For T-SbP monolayer, the variation of free energy during the AIMD simulation. Insets show the final structures (top view (a) and side view (b)) after 8 ps at 300 K.

that the T-XY ($X \neq Y = \text{P, As and Sb}$) monolayers are excellent 2D piezoelectric materials. Especially, the in-plane piezoelectric coefficient d_{11} (absolute value) of T-SbP is up to 226.15 pm/V, providing possibility of tuning spin-splitting of PSH by piezoelectric effect.

The rest of the paper is organized as follows. In the next section, we shall give our computational details and methods. In the next few sections, we shall present crystal structure and stability, electronic structures and persistent spin helix, and Piezoelectric properties of T-XY ($X \neq Y = \text{P, As and Sb}$) monolayers. Finally, we shall give our conclusion.

II. COMPUTATIONAL DETAIL

Within density functional theory (DFT)⁴², the first-principle calculations are carried out by using the projector augmented wave (PAW) method as implemented in Vienna ab initio Simulation Package (VASP)^{43–45}. We use the generalized gradient approximation of Perdew, Burke and Ernzerhof (GGA-PBE)⁴⁶ as exchange-correlation functional. The SOC is included to investigate electronic structures and PSH of T-XY ($X \neq Y = \text{P, As and Sb}$). The energy cut-off of 500 eV, total energy convergence criterion of 10^{-7} eV and force convergence criteria of $0.001 \text{ eV} \cdot \text{\AA}^{-1}$ are set to perform the first-principles calculations. A vacuum space of more than 28 Å between slabs along the z direction is added to eliminate the spurious interactions. A $3 \times 5 \times 1$ supercell is used to calculate the phonon spectrum within the finite displacement method by using the Phonopy code⁴⁷. The elastic stiffness (C_{ij}) are obtained by strain-stress relationship (SSR), and the piezoelectric stress tensors (e_{ij}) are calculated by using density functional perturbation theory (DFPT) method⁴⁸. The $2D C_{ij}^{2D}/e_{ij}^{2D}$ have been renormalized by $C_{ij}^{2D} = L_z C_{ij}^{3D}/e_{ij}^{2D} = L_z e_{ij}^{3D}$, where L_z is the length of unit cell along z direction. The constant energy contour plots of the spin texture are calculated by the PYPROCAR code⁴⁹. A $9 \times 18 \times 1$ k-point meshes in the first Brillouin zone (BZ) are adopted for all calculations.

TABLE I. For T-XY ($X \neq Y = \text{P, As and Sb}$) monolayer, the lattice constants a_0 and b_0 (Å), the elastic constants C_{ij} (Nm⁻¹), the piezoelectric coefficients e_{ij} (10⁻¹⁰ C/m) and d_{ij} (pm/V).

Name	a_0	b_0	C_{11}	C_{12}	C_{22}	C_{66}	e_{11}	e_{12}	e_{26}	d_{11}	d_{12}	d_{26}
AsP	9.38	3.48	9.87	10.72	77.64	18.97	-1.217	0.612	0.062	-15.52	2.93	0.33
SbP	8.95	3.83	3.50	9.19	60.04	17.71	-5.430	0.975	-1.889	-266.15	42.38	-10.66
SbAs	9.66	3.94	7.12	11.02	55.07	13.33	-1.898	0.778	-0.135	-41.82	9.78	-1.01

III. CRYSTAL STRUCTURE AND STABILITY

Similar to the α -phase, the T-phase MZ ($M = \text{Sn and Ge}$; $Z = \text{S and Se}$) has been proposed with excellent thermal, dynamical and mechanical stabilities, which exhibits C_{2v} symmetry and fold characteristics similar to "triple-staggered layers"⁴¹. The number of valence electrons remains constant, and the T-XY ($X \neq Y = \text{P, As and Sb}$) monolayer is constructed, including T-AsP, T-SbP and T-SbAs. The top and side views of crystal structures of T-XY are shown in Figure 1 (a) and (b). The primitive cell contains eight atoms, including four X atoms and four Y atoms, and each X (Y) atom is connected to three surrounding Y (X) atoms. Their optimized lattice parameters a and b along the x and y directions are listed in Table I.

The T-phase has four symmetry operations: (i) identity operation E ; (ii) twofold screw rotation \bar{C}_{2x} ; (iii) glide reflection \bar{M}_{xy} ; and (iv) reflection \bar{M}_{xz} with respect to the xz plane. The \bar{C}_{2x} is performed by twofold rotation around the x axis (C_{2x}), followed by translation of $\tau = a/2, b/2$. The \bar{M}_{xy} can be obtained by reflection with respect to the xy plane followed by translation τ . The T-phase lacks inversion symmetry, allowing piezoelectric response. Because the three T-XY monolayers share similar behavior, in the following, we shall mainly focus on T-SbP monolayer due to its large spin-splitting and piezoelectric response. The results of T-AsP and T-SbAs monolayers are briefly mentioned or put in FIG.1, FIG.2, FIG.3 and FIG.4 of the Supplementary Information (ESI).

To verify their dynamical stabilities, their phonon dispersions are calculated. Figure 1 (d) plots the result for monolayer SbP, which shows no imaginary frequency, indicating that the structure is dynamically stable. To investigate the thermal stability, the ab-initio molecular dynamics (AIMD) simulations are performed with a $2 \times 4 \times 1$ supercell and a time step of 1 fs. Figure 2 shows the simulation result on monolayer T-SbP at 300 K for 8 ps. One observes that the energy fluctuates within a small range during the whole simulation time, and the overall structure is well maintained at this temperature, indicating its good thermal stability. The linear elastic constants are calculated to determine their mechanical stabilities. Due to C_{2v} symmetry, four independent elastic constants (C_{11} , C_{12} , C_{22} and C_{66}) can be observed, which are listed in Table I. These C_{ij} meet Born-Huang criteria of mechanical stability ($C_{11} > 0$, $C_{66} > 0$ and $C_{11} * C_{22} > C_{12}^2$)⁵⁰, thereby verifying their mechanical

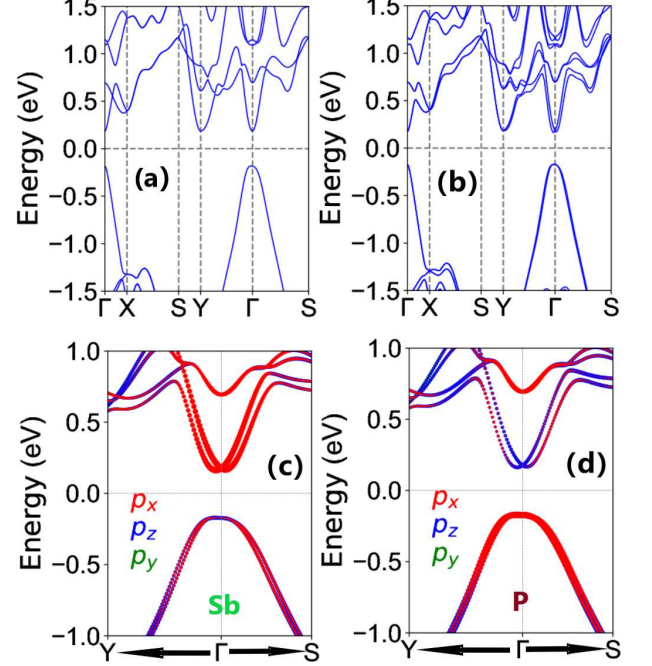


FIG. 3. (Color online) For T-SbP, the energy band structures without SOC (a) and with SOC (b). Zoom-in on the energy band structures around Γ point along Γ -Y and Γ -S lines with projected Sb (c) and P (d) atomic p -orbitals.

stabilities. The direction-dependent Young's modulus $C_{2D}(\theta)$ can be obtained as⁵¹:

$$C_{2D}(\theta) = \frac{C_{11}C_{22} - C_{12}^2}{C_{11} \sin^4 \theta + A \sin^2 \theta \cos^2 \theta + C_{22} \cos^4 \theta}, \quad (1)$$

where θ is the polar angle measured from x , and $A = (C_{11}C_{22} - C_{12}^2)/C_{66} - 2C_{12}$. According to FIG.5 of ESI, obvious anisotropy of elasticity is observed in the T-XY monolayers. The Young's modulus of AsP/SbP/SbAs along x direction is 8.39/2.09/4.92 Nm⁻¹, which is very smaller than one (66.00/35.91/38.01 Nm⁻¹) along the y direction. This indicates that the T-XY is more flexible and deformable along x direction, which plays a positive effect on their piezoelectricity.

IV. ELECTRONIC STRUCTURES AND PERSISTENT SPIN HELIX

Figure 3 shows the energy band structures of T-SbP calculated along high-symmetry k paths, and the ones

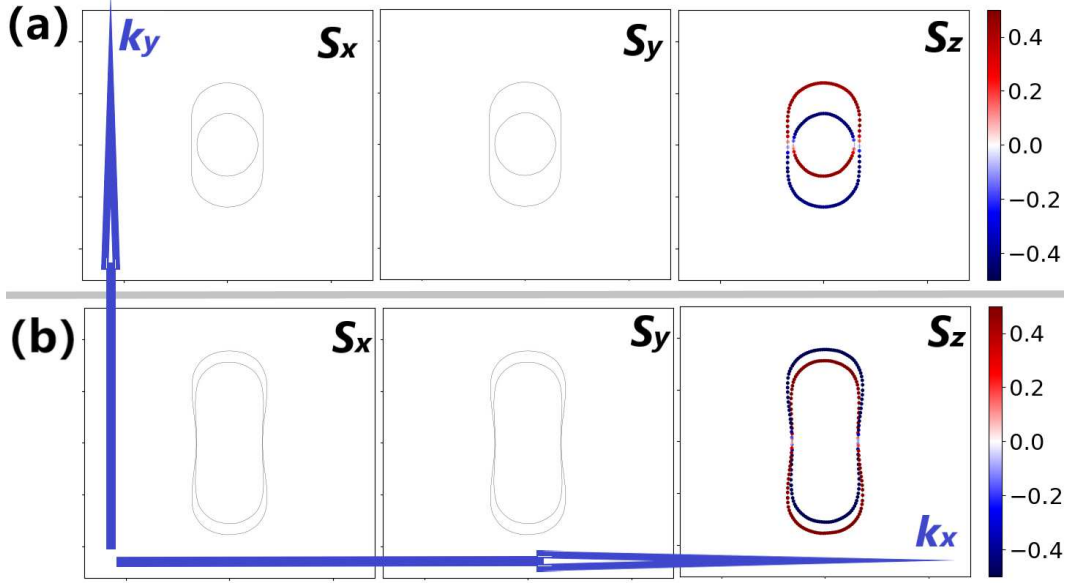


FIG. 4. (Color online) For T-SbP monolayer, the (a) [(b)] shows the spin texture (S_x , S_y and S_z) calculated in a $k_x - k_y$ plane centered at the Γ point with the isoenergetic surface of 0.25 [-0.25] eV above [below] the Fermi level. The color scale show the modulus of the spin polarization.

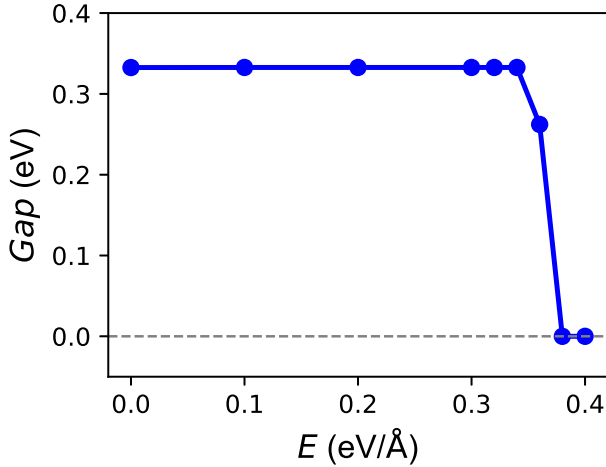


FIG. 5. (Color online) For T-SbP monolayer, the energy band gap as a function of out-of-plane external electric field E .

of the other two are plotted in FIG.3 and FIG.4 of ESI. Without including the SOC, the SbP is an indirect bandgap semiconductor, and the conduction band bottom (CBM) locates at Γ point, while the valence band maximum (VBM) slightly deviates from Γ along the Γ -Y path. However, the T-AsP and T-SbAs are direct bandgap semiconductors with both CBM and VBM at Γ point. The gaps of T-AsP, T-SbP and T-SbAs are 1.050 eV, 0.366 eV and 0.307 eV. When including the SOC, the energy band structures of T-XY are modified, and they all become indirect bandgap semiconductors with both CBM and VBM slightly deviating from Γ point. The gaps of T-AsP, T-SbP and T-SbAs become 1.047

eV, 0.332 eV and 0.289 eV. Importantly, a sizable splitting of the bands produced by the SOC is observed, especially for T-SbP monolayer. This splitting is especially pronounced around the Γ point near both the VBM and CBM. According to Figure 3 (c) and (d), the Sb- p_x and P- p_z orbitals contribute dominantly to the CBM, while the VBM are mainly from the contributions of the Sb- p_z and P- p_x orbitals.

For T-SbP monolayer, the Figure 4 (a) [(b)] shows the spin textures of conduction [valence] band calculated in a $k_x - k_y$ plane centered at the Γ point with the isoenergetic surface of 0.25 [-0.25] eV above [below] the Fermi level. It is clearly seen that the spin polarization is originated from the out-of-plane component S_z , while the in-plane component of spins (S_x and S_y) is zero. This means that the spin textures are unidirectional, which is very different from the in-plane Rashba spin textures. Such a spin texture produces a unidirectional out-of-plane SOF, resulting in a persistent spin texture (PST). The unidirectional SOF is robust against spin-independent scattering due to the PSH state, which leads to an extremely long spin lifetime by suppressing the Dyakonov-Perel spin-relaxation mechanism⁶.

To explain the PST with only out-of-plane component S_z , we establish an effective $k \cdot p$ Hamiltonian expanded at Γ point. The twofold degeneracy at Γ corresponds to the Γ_5 double-valued irreducible representation of C_{2v} . Taking the two states as basis, the generators, C_{2x} and M_{xy} , are represented in the matrix form as

$$\begin{aligned} D(C_{2x}) &= -i\sigma_x \\ D(M_{xy}) &= -i\sigma_z \\ D(T) &= -i\sigma_y\mathcal{K} \end{aligned} \quad (2)$$

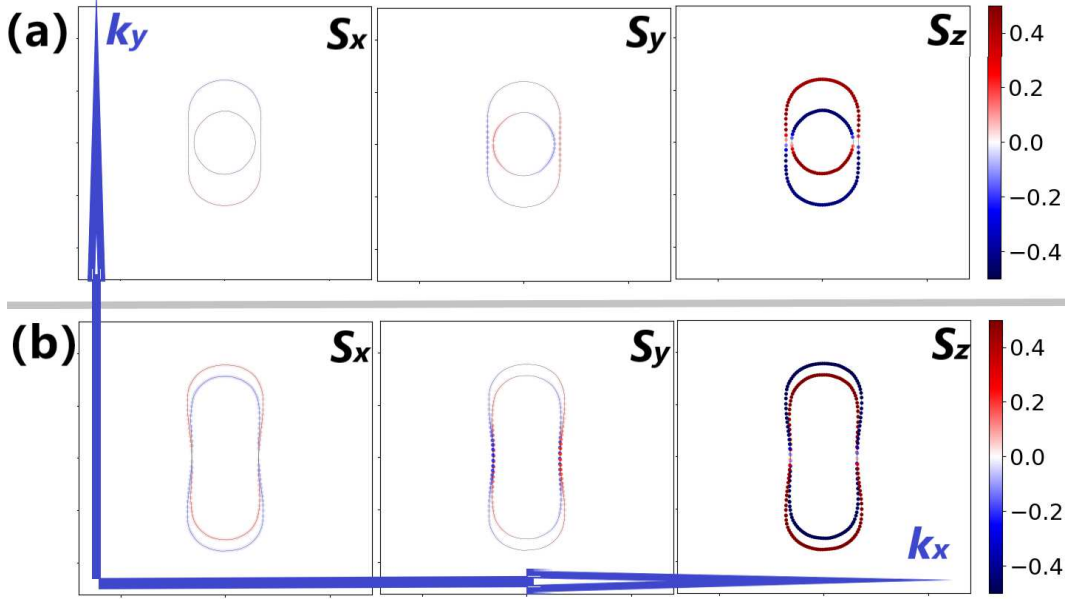


FIG. 6. (Color online) For T-SbP monolayer at $E=0.30$ V/Å, the (a) [(b)] shows the spin texture (S_x , S_y and S_z) calculated in a $k_x - k_y$ plane centered at the Γ point with the isoenergetic surface of 0.25 [-0.25] eV above [below] the Fermi level. The color scale show the modulus of the spin polarization.

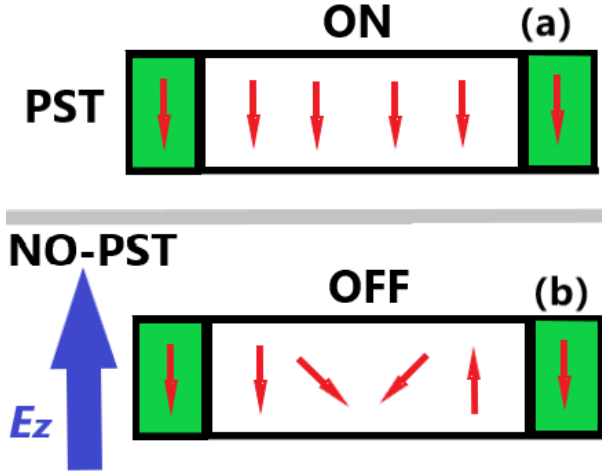


FIG. 7. (Color online) Schematic of spintronic devices: the red arrows represent spin, while the blue arrows represent out-of-plane electric field.

\mathcal{T} is time reversal symmetry operation. These symmetries constrain the Hamiltonian H by

$$\begin{aligned} C_{2x}H(\mathbf{k})C_{2x}^{-1} &= H(k_x, -k_y) \\ M_{xy}H(\mathbf{k})M_{xy}^{-1} &= H(k_x, k_y) \\ \mathcal{T}H(\mathbf{k})\mathcal{T}^{-1} &= H(-k_x, -k_y) \end{aligned} \quad (3)$$

Expanding $H(k)$ to k^3 order, the Hamiltonian can be written as:

$$H(k) = \alpha k_y \sigma_z + \alpha_1 k^2 \sigma_0 + (\alpha_2 k_y^3 + \alpha_3 k_x^2 k_y) \sigma_z \quad (4)$$

where σ_0 is 2×2 identity matrix, σ_z is the Pauli matrices, \vec{k} (k_x and k_y) is the wave vector, and α_i are model parameters. Since the spin operator S_z commutes with the Hamiltonian Equation 4, the spin operator S_z is a conserved quantity. The expectation value of the spin S only has the out-of-plane component, which produces the unidirectional out-of-plane spin configuration in k space.

On the other hand, by ignoring the high-order k items, the linear-term parameter α through the relation $\alpha = 2E_R/k_0$ can be obtained, where E_R and k_0 are the shifting energy and the wave vector along the y direction. The formation of the PSH mode should have a substantially small wavelength λ of the spin polarization. Here, the wavelength λ can be estimated by using $\lambda = \frac{\pi \hbar^2}{\alpha m^*}$, where m^* is the electron effective mass (Here, we only consider the conduction bands due to large spin-splitting.). The m^* is evaluated from the band dispersion along the Γ -Y line in the CBM. For several selected 2D PSH systems, the spin-splitting parameter α , effective mass m^* , and the wavelength of the spin polarization λ are summarized in Table II. This α of T-SbP is comparable with that reported for several 2D PSH systems, and the small wavelength of the PSH mode is typically on the scale of the lithographic dimension used in the recent semiconductor industry. Thus, the T-SbP should be promising for miniaturization of spintronic devices.

The application of the external electric field should modify the spin texture of T-SbP. So, an external out-of-plane electric field E is applied, which breaks both the C_{2x} rotational and M_{xy} in-plane mirror symmetries. The gap of T-SbP as a function of E is plotted in Figure 5, and the related energy band structures are shown in FIG.6 of ESI. It is clearly seen that the gap basically

TABLE II. For several selected 2D PSH systems, spin-splitting parameter α (eV·Å), effective mass m^* (m_0), and the wavelength of the spin polarization λ (nm).

Monolayer	α	m^*	λ	Reference
AsP	0.059	0.120	67.675	This work
SbP	1.103	0.116	3.745	This work
SbAs	0.454	0.092	11.471	This work
SnS	0.09	-	150	Ref. ²⁵
SnSe	0.74	-	44.85	Ref. ²⁵
SnTe	1.20	0.056	7.13	Ref. ²⁵
GeS	0.071	-	890	Ref. ²⁵
GeSe	0.57	-	91.84	Ref. ²⁵
GeTe	1.67	-	1.82	Ref. ²⁵
GaSeCl	1.2	-	2.89	Ref. ²¹
GaSeBr	0.85	-	4.09	Ref. ²¹
GaSeI	0.53	-	6.57	Ref. ²¹
GaTeCl	2.65	-	1.20	Ref. ²¹
GaTeBr	2.40	-	1.45	Ref. ²¹
GaTeI	1.90	-	1.83	Ref. ²¹

remains unchanged, when E is less than about 0.34 V/Å. At about $E=0.38$ V/Å, a semiconductor-to-metal phase transition can be observed.

Under the out-of-plane external electric field, the effective Rashba contribution should be added in Hamiltonian Equation 4, which has the isotropic form¹:

$$H_R^{iso} = \alpha_R^{iso} (k_x \sigma_y - k_y \sigma_x) \quad (5)$$

The introducing Rashba term will induce the in-plane spin components due to the broken in-plane mirror symmetry M_{xy} caused by the out-of-plane external electric field. To confirm this, the Figure 6 (a) [(b)] shows the spin textures of conduction [valence] band calculated in a $k_x - k_y$ plane centered at the Γ point with the isoenergetic surface of 0.25 [-0.25] eV above [below] the Fermi level for T-SbP at $E=0.30$ V/Å. It is clearly observed that significant in-plane spin components (S_x and S_y) are induced, thus breaking the PST and perturbs the PSH state.

The in-plane spin components can be turned on by applied out-of-plane electric field, which provides a possibility of the on-off logical functionality of spin devices by controlling the passage of electrons (see Figure 7). For example, two ferromagnetic (FM) electrodes in the same direction are set for source and drain electrodes. Without the out-of-plane electric field, the out-of-plane orientation of the spin polarization injected from the source electrode maintains due to PST, when the injected electrons pass through the T-SbP channel (Figure 7 (a)). When the external electric field is applied, the PST is broken, and the PSH state is perturbed. The spin of electrons in the channel will rotate, and will be blocked by the drain electrode (Figure 7 (b)). The function of spintronic switch can be realized in the possible spintronic device.

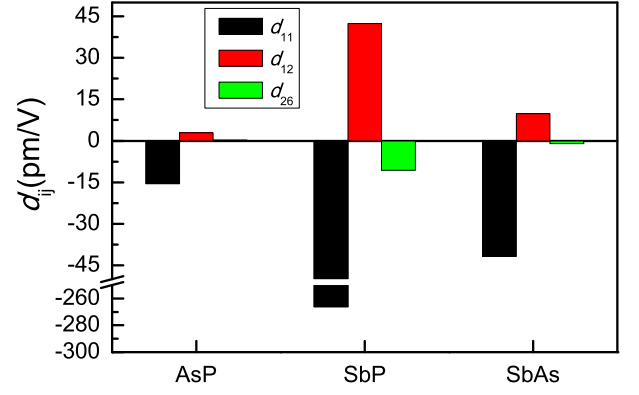


FIG. 8. (Color online) For T-XY ($X \neq Y = \text{P, As and Sb}$) monolayer, the piezoelectric strain coefficients d_{11} , d_{12} and d_{26} .

V. PIEZOELECTRIC PROPERTIES

When a material lacks central inversion symmetry, the electric dipole moments (producing electricity) can be induced by an applied strain or stress, called piezoelectric effect. The T-XY ($X \neq Y = \text{P, As and Sb}$) monolayers lack M_{yz} mirror symmetry, which induces the in-plane piezoelectric effect. The piezoelectric response of a material can be described by the third-rank piezoelectric stress tensor e_{ijk} and strain tensor d_{ijk} . The relaxed piezoelectric tensors (e_{ijk} and d_{ijk}) as the sum of ionic and electronic contributions can be expressed as:

$$\begin{aligned} e_{ijk} &= \frac{\partial P_i}{\partial \varepsilon_{jk}} = e_{ijk}^{elc} + e_{ijk}^{ion} \\ d_{ijk} &= \frac{\partial P_i}{\partial \sigma_{jk}} = d_{ijk}^{elc} + d_{ijk}^{ion} \end{aligned} \quad (6)$$

Where P_i , ε_{jk} and σ_{jk} are polarization vector, strain and stress, respectively. The electronic and ionic contributions are marked by superscripts *elc* and *ion*. The e_{ijk}^{elc} and d_{ijk}^{elc} are also called clamped-ion piezoelectric coefficients, and the e_{ijk} and d_{ijk} for relax-ion piezoelectric coefficients. The e_{ijk} and d_{ijk} are related by elastic tensor C_{mnjk} :

$$e_{ijk} = \frac{\partial P_i}{\partial \varepsilon_{jk}} = \frac{\partial P_i}{\partial \sigma_{mn}} \cdot \frac{\partial \sigma_{mn}}{\partial \varepsilon_{jk}} = d_{imn} C_{mnjk} \quad (7)$$

For 2D materials, only the in-plane strain and stress are taken into account ($\varepsilon_{ij} = \sigma_{ij} = 0$ for $i=3$ or $j=3$)^{28,30-38}, but the polarization can be allowed to remain out-of-plane. As shown in Figure 1, the long edge and short edge of primitive cell are defined as the in-plane directions x and y , and z is perpendicular to the monolayer. By employing Voigt notation, due to C_{2v} point group symmetry, the Equation 7 can be reduced into⁴¹:

$$\begin{pmatrix} e_{11} & e_{12} & 0 \\ 0 & 0 & e_{26} \\ 0 & 0 & 0 \end{pmatrix} = \begin{pmatrix} d_{11} & d_{12} & 0 \\ 0 & 0 & d_{26} \\ 0 & 0 & 0 \end{pmatrix} \begin{pmatrix} C_{11} & C_{12} & 0 \\ C_{12} & C_{22} & 0 \\ 0 & 0 & C_{66} \end{pmatrix} \quad (8)$$

With an applied uniaxial in-plane strain, only an in-plane piezoelectric polarization along x direction exists ($d_{11} \neq 0$ or $d_{12} \neq 0$). Moreover, when a biaxial in-plane strain is applied, the d_{11} and d_{12} simultaneously appear. By an applied shear strain, the in-plane piezoelectric polarization along y direction exists ($d_{26} \neq 0$). The e_{11} , e_{12} and e_{26} can be directly calculated by DFPT, and the d_{11} , d_{12} and d_{26} can be derived by Equation 8:

$$\begin{aligned} d_{11} &= \frac{e_{11}C_{22} - e_{12}C_{12}}{C_{11}C_{22} - C_{12}^2} \\ d_{12} &= \frac{e_{12}C_{11} - e_{11}C_{12}}{C_{11}C_{22} - C_{12}^2} \\ d_{26} &= \frac{e_{26}}{C_{66}} \end{aligned} \quad (9)$$

The orthorhombic primitive cell is used to calculate the e_{ij} of T-XY ($X \neq Y = \text{P, As and Sb}$) monolayer. The piezoelectric stress coefficients (e_{ij}) along the ionic and electronic contributions are plotted in FIG.7 of ESI. For the three monolayers, the electronic and ionic parts of e_{11} have superposed contributions, and the ionic part is larger than electronic one (absolute value). However, the electronic and ionic contributions of e_{12} and e_{26} have opposite signs. For e_{12} , the electronic part dominates the piezoelectricity. For e_{26} , the ionic part dominates the piezoelectricity except for T-AsP monolayer. And then, the d_{ij} of T-XY can be calculated from Equation 9, which are shown in Figure 8. The e_{ij} and d_{ij} also summarized in Table I. It is found that the three d_{ij} of T-SbP are all very larger than ones of T-AsP and T-SbAs. For the three monolayers, the d_{11} (absolute values) is very larger than d_{12} and d_{26} due to a remarkable small elastic constant C_{11} along the x direction, indicating the anisotropic piezoelectric property of T-XY. Interestingly, the d_{11} (absolute value) of T-XY is larger than that for most previously reported 2D piezoelectric materials^{28,30-38}. Moreover, the d_{11} of T-SbP is as high as 266.15 pm/V, which plays a positive effect on tuning spin-splitting by piezoelectric effect.

A general form of the SOC Hamiltonian H_{SOC} in solid-state materials can be expressed as^{39,40}:

$$H_{SOC} = \alpha'(\vec{E} \times \vec{k}) \cdot \vec{\sigma} \quad (10)$$

where α' is the strength of the SOC, and $\vec{\sigma} = (\sigma_x, \sigma_y, \sigma_z)$ are the Pauli matrices, and \vec{E} is electric field. For T-SbP,

the spontaneous in-plane electric polarization is oriented along x direction. The Equation 10 is written as:

$$H_{SOC} = \alpha k_y \sigma_z \quad (11)$$

This is consistent with Equation 4, when ignoring the higher order terms of k . The α is proportional to the magnitude of the built-in electric field. The electric field along x direction can also be induced with a uniaxial in-plane strain by piezoelectric effect, and then tune spin-splitting of T-SbP. When a uniaxial in-plane vibration is applied to T-SbP, the spin-splitting will be modulated periodically. For example, the compressive strain produce negative electric field, and then reduce spin-splitting of PST. However, the tensile strain induces positive electric field, and then enhances spin-splitting of PST.

VI. CONCLUSION

In summary, based on first-principles calculations along with symmetry analysis, we systematically investigated the electronic and piezoelectric properties of T-XY ($X \neq Y = \text{P, As and Sb}$) monolayers with dynamical, mechanical and thermal stabilities. Because of C_{2v} point-group symmetry, the unidirectional out-of-plane spin configurations are preserved in T-XY ($X \neq Y = \text{P, As and Sb}$) monolayers, giving rise to the PSH state. It is found that this PSH is observed near both VBM and CBM around Γ point. The out-of-plane electric field can be used to perturb PSH, which provides possibility to realize electronic device of switching function. The in-plane intrinsic piezoelectric coefficient d_{11} of T-XY ($X \neq Y = \text{P, As and Sb}$) monolayers exceed those reported for most 2D compounds, which mainly stems from its extraordinarily flexible configurations along the polarization direction. The in-plane intrinsic piezoelectric properties can be used to tune spin-splitting of PSH. Our work reveals a new 2D family of materials that have great potential for spintronic and piezoelectric device applications.

ACKNOWLEDGMENTS

This work was supported by Natural Science Basis Research Plan in Shaanxi Province of China (No. 2021JM-456). We are grateful to Shanxi Supercomputing Center of China, and the calculations were performed on TianHe-2.

¹ E. I. Rashba, Sov. Phys. Solid State **2**, 1224 (1960).

² G. Dresselhaus, Phys. Rev. **100**, 580 (1955).

³ J. Nitta, T. Akazaki, H. Takayanagi, and T. Enoki, Phys. Rev. Lett. **78**, 1335 (1997).

⁴ A. Manchon, H. C. Koo, J. Nitta, S. M. Frolov, and R. A. Duine, Nat. Mater. **14**, 871 (2015).

⁵ P. Chuang, S. H. Ho, L. W. Smith et al., Nat. Nanotechnol. **10**, 35 (2009).

⁶ M. I. Dyakonov and V. I. Perel, Sov. Phys. Solid State **13**, 3023 (1972).

⁷ B. A. Bernevig, J. Orenstein, and S.-C. Zhang, Phys. Rev. Lett. **97**, 236601 (2006).

- ⁸ J. Schliemann, *Rev. Mod. Phys.* **89**, 011001 (2017).
- ⁹ P. Altmann, M. P. Walser, C. Reichl, W. Wegscheider, and G. Salis, *Phys. Rev. B* **90**, 201306(R) (2014).
- ¹⁰ J. D. Koralek, C. P. Weber, J. Orenstein, B. A. Bernevig, S.-C. Zhang, S. Mack, and D. D. Awschalom, *Nature (London)* **458**, 610 (2009).
- ¹¹ M. P. Walser, C. Reichl, W. Wegscheider, and G. Salis, *Nat. Phys.* **8**, 757 (2012).
- ¹² J. Ishihara, Y. Ohno, and H. Ohno, *Appl. Phys. Express* **7**, 013001 (2014).
- ¹³ M. Kohda, V. Lechner, Y. Kunihashi et al., *Phys. Rev. B* **86**, 081306(R) (2012).
- ¹⁴ A. Sasaki, S. Nonaka, Y. Kunihashi, M. Kohda, T. Bauernfeind, T. Dollinger, K. Richter, and J. Nitta, *Nat. Nanotechnol.* **9**, 703 (2014).
- ¹⁵ N. Yamaguchi and F. Ishii, *Appl. Phys. Express* **10**, 123003 (2017).
- ¹⁶ M. A. U. Absor, F. Ishii, H. Kotaka, and M. Saito, *Appl. Phys. Express* **8**, 073006 (2015).
- ¹⁷ L. L. Tao and E. Y. Tsymlal, *Nat. Commun.* **9**, 2763 (2018).
- ¹⁸ C. Autieri, P. Barone, J. Slawińska and S. Picozzi, *Phys. Rev. Materials* **3**, 084416 (2019).
- ¹⁹ H. Djani, A. C. Garcia-Castro, W. Y. Tong, P. Barone, E. Bousquet, S. Picozzi and P. Ghosez, *npj Quant. Mater.* **4**, 51 (2019).
- ²⁰ H. Ai, X. Ma, X. Shao, W. Li and M. Zhao, *Phys. Rev. Materials* **3**, 054407 (2019).
- ²¹ S. A. Sasmito, M. Anshory, I. Jihad and M. A. U. Absor, *Phys. Rev. B* **104**, 115145 (2021).
- ²² M. A. U. Absor and F. Ishii, *Phys. Rev. B* **103**, 045119 (2021).
- ²³ F. Jia, S. Hu, S. Xu, H. Gao, G. Zhao, P. Barone, A. Stroppa and W. Ren, *J. Phys. Chem. Lett.* **11**, 5177 (2020).
- ²⁴ M. A. U. Absor and F. Ishii, *Phys. Rev. B* **99**, 075136 (2019).
- ²⁵ M. A. U. Absor and F. Ishii, *Phys. Rev. B* **100**, 115104 (2019).
- ²⁶ H. Lee, J. Im and H. Jin, *Appl. Phys. Lett.* **116**, 022411 (2020).
- ²⁷ H. J. Zhao, H. Nakamura, R. Arras, C. Paillard, P. Chen, J. Gosteau, X. Li, Y. Yang and L. Bellaiche, *Phys. Rev. Lett.* **125**, 216405 (2020).
- ²⁸ K. N. Duerloo, M. T. Ong and E. J. Reed, *J. Phys. Chem. Lett.* **3**, 2871 (2012).
- ²⁹ W. Wu, L. Wang, Y. Li, F. Zhang, L. Lin, S. Niu, D. Chenet, X. Zhang, Y. Hao, T. F. Heinz, J. Hone and Z. L. Wang, *Nature* **514**, 470 (2014).
- ³⁰ L. Dong, J. Lou and V. B. Shenoy, *ACS Nano*, **11**, 8242 (2017).
- ³¹ Y. Xu, Z. Q. Li, C. Y. He, J. Li, T. Ouyang, C. X. Zhang, C. Tang and J. X. Zhong, *Appl. Phys. Lett.* **116**, 023103 (2020).
- ³² M. N. Blonsky, H. L. Zhuang, A. K. Singh and R. G. Hennig, *ACS Nano* **9**, 9885 (2015).
- ³³ S. D. Guo, Y. T. Zhu, W. Q. Mu and W. C. Ren, *EPL* **132**, 57002 (2020).
- ³⁴ R. X. Fei, W. B. Li, J. Li and L. Yang, *Appl. Phys. Lett.* **107**, 173104 (2015).
- ³⁵ K. N. Duerloo, M. T. Ong and E. J. Reed, *J. Phys. Chem. Lett.* **3**, 2871 (2012).
- ³⁶ N. Jena, Dimple, S. D. Behere and A. D. Sarkar, *J. Phys. Chem. C* **121**, 9181 (2017).
- ³⁷ Y. Chen, J. Y. Liu, J. B. Yu, Y. G. Guo and Q. Sun, *Phys. Chem. Chem. Phys.* **21**, 1207 (2019).
- ³⁸ S.-D. Guo, X.-K. Feng, Y.-T. Zhu, G. Z. Wang and S. Y. A. Yang, *Phys. Chem. Chem. Phys.* **25**, 2274 (2023).
- ³⁹ J. Nitta, T. Akazaki, H. Takayanagi, and T. Enoki, *Phys. Rev. Lett.* **78**, 1335 (1997).
- ⁴⁰ A. Manchon, H. C. Koo, J. Nitta, S. M. Frolov, and R. A. Duine, *Nat. Mater.* **14**, 871 (2015).
- ⁴¹ H. Lei, T. Ouyang, C. Y. He, J. Li and C. Tang, *Appl. Phys. Lett.* **122**, 062903 (2023).
- ⁴² P. Hohenberg and W. Kohn, *Phys. Rev.* **136**, B864 (1964); W. Kohn and L. J. Sham, *Phys. Rev.* **140**, A1133 (1965).
- ⁴³ G. Kresse, *J. Non-Cryst. Solids* **193**, 222 (1995).
- ⁴⁴ G. Kresse and J. Furthmüller, *Comput. Mater. Sci.* **6**, 15 (1996).
- ⁴⁵ G. Kresse and D. Joubert, *Phys. Rev. B* **59**, 1758 (1999).
- ⁴⁶ J. P. Perdew, K. Burke and M. Ernzerhof, *Phys. Rev. Lett.* **77**, 3865 (1996).
- ⁴⁷ A. Togo, F. Oba, and I. Tanaka, *Phys. Rev. B* **78**, 134106 (2008).
- ⁴⁸ X. Wu, D. Vanderbilt and D. R. Hamann, *Phys. Rev. B* **72**, 035105 (2005).
- ⁴⁹ U. Herath, P. Tavazze, X. He, E. Bousquet, S. Singh, F. Munoz and A. H. Romero, *Comput. Phys. Commun.* **251**, 107080 (2020).
- ⁵⁰ M. Born and K. Huang, *Am. J. Phys.* **23**, 474 (1995).
- ⁵¹ E. Cadelano, P. L. Palla, S. Giordano and L. Colombo, *Phys. Rev. B* **82**, 235414 (2010).